Journal of Materials Chemistry C

Atypical phase-change alloy Ga2Te3: atomic structure, incipient nanotectonic nuclei, multilevel writing

Journal:	*Journal of Materials Chemistry C*
Manuscript ID	TC-ART-08-2021-003850.R2
Article Type:	Paper
Date Submitted by the Author:	04-Nov-2021

Complete List of Authors:	Tverjanovich, Andrey; St. Petersburg State University, Department of Chemistry Khomenko, Maxim; ILIT RAS – Branch of the FSRC 'Crystallography and Photonics Benmore, Chris; Argonne National Laboratory, Bereznev, Sergei; Tallinn University of Technology Sokolov, Anton; Univ. Littoral Côte d'Opale, LPCA, EA CNRS 4493 Fontanari, Daniele; Universite du Littoral Cote D'Opale Kiselev, Aleksei; ILIT RAS – Branch of the FSRC 'Crystallography and Photonics' RAS Lotin, Andrey; ILIT RAS – Branch of the FSRC 'Crystallography and Photonics' RAS Bychkov, Eugene; University of Littoral, LPCA

Atypical phase-change alloy Ga_2Te_3: atomic structure, incipient nanotectonic nuclei, multilevel writing†

Andrey Tverjanovich,[a] Maxim Khomenko,[b] Chris J. Benmore,[c] Sergei Bereznev,[d] Anton Sokolov,[be] Daniele Fontanari,[e] Aleksei Kiselev,[b] Andrey Lotin[b] and Eugene Bychkov[be]*

Emerging brain-inspired computing, including artificial optical synapses, photonic tensor cores, neuromorphic networks, etc., needs phase-change materials (PCMs) of the next generation with lower energy consumption and wider temperature range for reliable long-term operation. Gallium tellurides with higher melting and crystallization temperatures appear to be promising candidates enable to achieve the necessary requirements. Using high energy X-ray diffraction and Raman spectroscopy supported by first-principles simulations, we show that vitreous g-Ga_2Te_3 films essentially have a tetrahedral local structure and the sp^3 hybridization, similar to those in the stable fcc Ga_2Te_3 polymorph and in opposite to a vast majority of typical PCMs. Nevertheless, optical pump-probe laser experiments revealed high-contrast, fast and reversible multilevel SET-RESET transitions raising a question of the phase change mechanism. A recently observed nanotectonic compression in bulk glassy Ga-Te alloys seems to be responsible for the PCM performance. Incipient nanotectonic nuclei, reminiscent of monoclinic high-pressure HP-Te II and rhombohedral HP-Ga_2Te_3, are present as minorities (2-4%) in g-Ga_2Te_3 but suggested to grow dramatically with increasing temperature while interacting with appropriate laser pulses. This leads to a co-crystallization of HP-polymorphs amplified by high internal local pressure reaching 4-8 GPa. The metallic HP-forms provide an increasing optical and electrical contrast, favorable for reliable PCM operations, and higher energy efficiency.

[a] *Institute of Chemistry, St. Petersburg State University, 198504 St. Petersburg, Russia*
[b] *ILIT RAS – Branch of the FSRC 'Crystallography and Photonics' RAS, 140700 Shatura, Moscow Region, Russia*
[c] *X-ray Science Division, Advanced Photon Source, Argonne National Laboratory, Argonne, Illinois 60439, United States*
[d] *Department of Materials and Environmental Technology, Tallinn University of Technology, 19086 Tallinn, Estonia*
[e] *Laboratoire de Physico-Chimie de l'Atmosphère, Université du Littoral Côte d'Opale, 59140 Dunkerque, France. E-mail: bychkov@univ-littoral.fr*

† Electronic supplementary information (ESI) available: homopolar and heteropolar bond energies in the Ga-Te system; rough estimation of optical properties of crystallized and amorphous Ga_2Te_3; schematics of the experimental pump-probe setup; electronic density of states in bulk glassy $GaTe_4$ at 300 K; optical RESET–SET transition in Ga_2Te_3 PLD film induced by a femtosecond laser; crystal structure of rhombohedral Ga_2Te_3; neutron total correlation functions of rhombohedral and cubic Ga_2Te_3; structural changes during SET-RESET transitions. See DOI:

1 Introduction

Neuromorphic computing using phase change materials (PCMs)[1-4] appears to be a promising alternative to the classical von Neumann computer architecture.[5-7] Further development of neuromorphic systems will need improvements in energy efficiency and a wider temperature range for reliable operations. PCMs based on gallium tellurides appear to be promising candidates enable to achieve the necessary requirements. Gallium sesquitelluride Ga_2Te_3 has higher melting and crystallization temperatures compared to flagship PCMs (GeTe, $Ge_2Sb_2Te_5$, doped Sb_2Te, etc.) and simultaneously a low switching power and fast switching rate.[8-10] At the same time, Ga_2Te_3 appears to be a very unusual phase-change alloy, combining a regular tetrahedral structure in the face-centered cubic polymorph,[11] the absence of Peierls distortion and resonant[12] or metavalent[13,14] bonding, typical for PCMs. The sp^3 gallium hybridization in fcc Ga_2Te_3 is also different from usual p-bonding in GeTe or $Ge_2Sb_2Te_5$. These features are raising a question related to the phase-change mechanism in gallium tellurides.

The reported atomic structure of liquid or amorphous gallium sesquitelluride is controversial. The early X-ray diffraction studies of liquid Ga_xTe_{1-x} alloys, $0 \le x \le 1$, have suggested a chemically ordered network but with a strong dissociation of Ga–Te units.[15] Consequently, the gallium local environment in stoichiometric ℓ-Ga_2Te_3 was reported to be mixed, $N_{Ga-X} \approx 3.5$, where X = Te or Ga, with comparable fractions of Ga-Te and Ga-Ga bonds. On the contrary, the results of neutron diffraction with isotopic substitution and anomalous X-ray scattering at the Te K edge have shown similar gallium local coordination, N_{Ga-Te} = 3.5 ± 0.5, however, without a substantial number of Ga–Ga and Te–Te homopolar bonds.[16] Recently reported EXAFS results for amorphous Ga_2Te_3 thin films, measured at the Ga and Te K edges, have revealed the tetrahedral gallium environment with a small fraction of Ga–Ga nearest neighbors, also confirmed by first-principles modeling.[17] Finally, our high-energy X-ray diffraction and Raman spectroscopy results of Te-rich bulk Ga_xTe_{1-x} glasses, $0.17 \le x \le 0.25$, supported by first-principles simulations of vibrational, structural and electronic properties, have validated the tetrahedral Ga coordination.[18] In addition, a very unusual phenomenon has been observed, the nanotectonic compression, consisting of co-crystallization of the stable ambient and metastable high-pressure (HP) polymorphic forms on usual heating of glassy $GaTe_3$ (x = 0.25) above the glass transition. The co-crystallization of metallic HP-polymorphs seems to be beneficial for the PCM performance, increasing the optical and electrical contrast between the SET (crystalline) and RESET (amorphous) logic states, thus decreasing the power consumption and enabling the multilevel writing.

The main objectives of the present report are (i) unraveling the atomic structure of vitreous Ga_2Te_3, obtained by pulsed laser deposition, using high-energy X-ray diffraction and Raman spectroscopy, supported by first-principles simulations; (ii) verifying the PCM performance of Ga_2Te_3 using optical pump-probe laser technique; and (iii) elucidating a possible phase-change mechanism.

2 Experimental and methods

2.1 Target synthesis and pulsed laser deposition

Gallium sesquitelluride target for pulsed laser deposition (PLD) was synthesized from high-purity elements: Ga (99.999%, Neyco) and Te (99.999%, Cerac). Flat bottom silica tubes (25 mm ID) with stoichiometric mixtures were sealed under vacuum (10^{-4} mbar) and placed into a rocking furnace. Maximum synthesis temperature was 1250 K. Homogenized and synthesized samples were slowly cooled in a furnace in horizontal position. Further target preparation was done in a vertical furnace with the same maximum temperature. The sample was held at 1250 K for 4 h and then very slowly cooled down to room temperature. The silica tube with polycrystalline Ga_2Te_3 was cut using a circular diamond saw blades. The final monolithic target had diameter 25 mm and thickness 7 mm. The X-ray diffraction pattern were found to be identical to face-centered cubic Ga_2Te_3.[11]

Ga_2Te_3 thin films were deposited at room temperature by PLD onto LCD grade float glass substrates (Kintec Company) with the substrate diameter of 2" and thickness of 1.1 mm. Prior to deposition, the substrates were cleaned ultrasonically in reagent grade methanol and in de-ionized water (Millipore) for 10 min. After cleaning, the substrates were dried under nitrogen flow and then subjected to NovaScan Digital UV-Ozone cleaning system for 15 min before loading in the deposition chamber of a Neocera PLD system equipped with a 248 nm KrF excimer laser (Coherent Compex 102 F). The laser beam was focused on a ≈5 mm^2 spot on the surface of the rotating target. The target to substrate distance was 9 cm while the pressure in vacuum chamber was around $4 \cdot 10^{-6}$ mbar without any specific background gas pressure. For preparation of the "thick" layers with the thickness above 1 μm we used 75000 laser pulses of 200 mJ pulse energy and 10 Hz repetition rate. The "thin" layers with the thickness around 100 nm were prepared at the following deposition parameters: 7300 laser pulses of 200 mJ pulse energy and 10 Hz repetition rate. The chemical composition of the PLD films was verified by energy dispersive X-ray spectroscopy and was found to be consistent with expectations: 40.7 ± 0.7 at.% Ga (K-series) and 59.3 ± 1.9 at.% Te (L-series).

2.2 Optical absorption and Raman spectroscopy measurements

Optical absorption spectra have been measured over a wide spectral region from the fundamental absorption edge of gallium sesquitelluride at $\lambda \approx 700$ nm to a long-wave limit of 5200 nm related to the phonon absorption of the glass substrate. A Shimadzu UV-3600 spectrophotometer was used for optical absorption measurements in the wavelength range of 500−3200 nm. A far-IR region was covered by a Bruker Tensor FTIR spectrometer, allowing the extended IR range up to 25 μm but limited by 6000 nm because of phonon absorption. The two instruments have overlapping spectral domains between 2500 and 3200 nm. After optical measurements of the Ga_2Te_3 PLD film on glass substrate, the thin film was removed from the substrate in alkaline solution. The optical absorption of the substrate was measured and subtracted from the Ga_2Te_3/glass total absorption.

Raman spectra were measured at room temperature in backscattering geometry using a Senterra Raman spectrometer (Bruker) equipped with a microscope. The spectra were excited by a 785 nm solid-state laser with a power of 1 mW using a low magnification objective (10×, NA 0.25) to avoid laser-induced crystallization or damage of the glass samples. The absence of possible deterioration effects was checked directly after measurements by optical microscopy.

2.3 Pump-probe phase-change experiments

An optical pump-probe experimental setup consisting of a nanosecond solid-state YAG:Nd^{3+} laser (λ_{pump} = 532 nm) and a low-power cw probing laser (λ_{probe} = 980 nm) was used for time-resolved phase-change experiments using 100 nm Ga_2Te_3 PLD films (Fig. S1, Electronic Supplementary Information). The samples were exposed to nanosecond laser pulses of variable energy density in either a single-pulse mode or using a multi-pulse train with the repetition rate of 10 Hz. Laser-induced phase-change transitions were studied using the reflectivity $\Delta R/R$ and/or transmission changes $\Delta T/T$. Further details of the pump-probe setup and time-resolved measurements were published previously.[19-21] A limited number of experiments were conducted using a femtosecond laser Astrella Coherent (λ_{pump} = 800 nm, the energy density 20 mJ cm^{-2}) and a 15 mW probing laser (λ_{probe} = 1550 nm).

2.4 High-energy X-ray diffraction measurements

Tiny pieces of gallium sesquitelluride thin film material were placed into a thin-walled silica capillary for high-energy X-ray diffraction measurements. The 6-ID-D beamline at the Advanced Photon Source (Argonne National Laboratory, Chicago) was used for these experiments with the photon energy of 99.9758 keV, and the wavelength of 0.124014 Å. A two-dimensional (2D) setup was used for data collection with a Varex area detector. The exposure time was 0.1 s × 3000 frames, using one dark-field image file followed by five light files. The 2D diffraction patterns were reduced using the Fit2D software.[22] The measured background intensity of the empty silica capillary was subtracted, and corrections were made for the different detector geometries and efficiencies, sample self-attenuation, and Compton scattering using standard procedures,[23] providing the X-ray structure factor $S_X(Q)$ for vitreous Ga_2Te_3.

2.5 Computational details

Modeling of the high-energy X-ray diffraction data was carried out using Born–Oppenheimer molecular dynamics implemented within the CP2K package.[24] The generalized gradient approximation (GGA) and the PBE0 hybrid[25,26] exchange–correlation functional combining the exact Hartree–Fock and density functional theory (DFT) approaches were used, providing a better agreement with experiment.[18,27-29] The van der Waals dispersion corrections D3BJ[30] were also applied, improving first-principles molecular dynamics (FPMD) results for telluride systems.[31,32]

The used FPMD technique was similar to that reported previously.[33,34] The initial atomic configurations for vitreous Ga_2Te_3 were created and optimized using the RMC_POT++ code[35]

against the experimental X-ray structure factor $S_X(Q)$. The size of the cubic simulation box at room temperature, containing 500 atoms (200 Ga and 300 Te), was chosen to match the experimental number density. Further optimization was carried out using DFT at 0 K, applying the molecularly optimized correlation consistent polarized triple-zeta valence basis set along with the norm-conserving relativistic Goedecker–Teter–Hutter-type pseudopotentials.[36] FPMD simulations were performed using a canonical NVT ensemble with a Nosé–Hoover[37,38] chain of length 3 as a thermostat. The simulation boxes were heated from 300 K to 1300 K using 200 K steps for 10–15 ps each. At 1300K, the systems were equilibrated for 53 ps and cooled down to 300 K using the same temperature steps but with a longer simulation time (≈30 ps). Final equilibration and data collection at 300 K were performed for 52 ps. The connectivity and ring statistics were analyzed using the R.I.N.G.S. package[39] and a modified connectivity program.[40] The pyMolDyn code[41] applying the Dirichlet–Voronoi tessellation was used for the calculation of microscopic voids and cavities.

3 Results and discussion

3.1 Optical properties

The uniformity of the Ga_2Te_3 PLD film was confirmed by optical absorption measurements with distinct interference fringes, Fig. 1(a). Using the Swanepoel method,[42] the layer thickness d and the refractive index n_R over the $1.1 \leq \lambda \leq 2.3$ μm spectral range were calculated from the transmission spectrum derived from the absorption. The calculated thickness d = 1.10 ± 0.06 μm was consistent with the PLD regime. The refractive index n_R = 3.13 ± 0.08, derived using the substrate refractive index n_S = 1.58, was similar to those reported previously.[43-45]

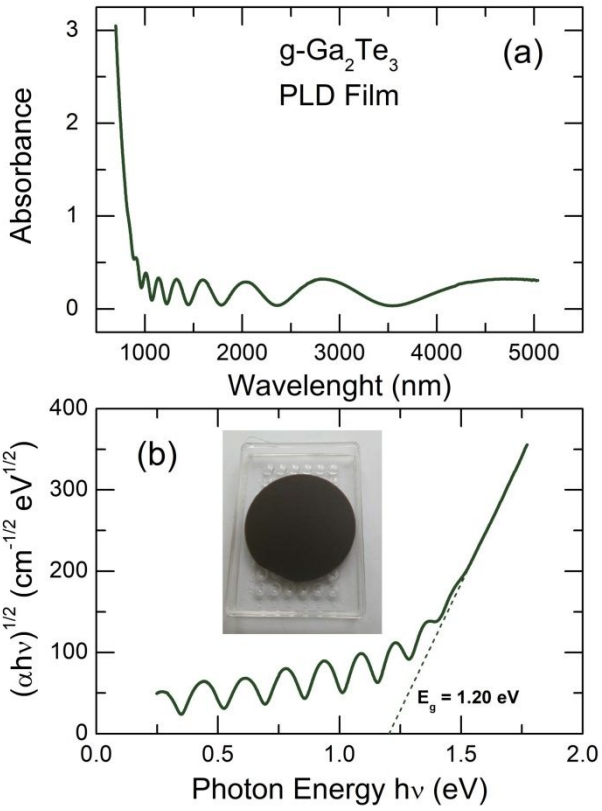

Fig. 1 Optical properties of vitreous Ga_2Te_3 PLD film: (a) optical absorbance with interference fringes, (b) the Tauc plot: $\sqrt{\alpha h\upsilon}$ vs photon energy $h\upsilon$, where α is the absorption coefficient, used to determine the optical band gap E_g. The inset shows a typical appearance of the Ga_2Te_3 PLD film.

The fundamental absorption range of vitreous gallium sesquitelluride starts below 900 nm. The calculated absorption coefficient α is shown in Fig. 1(b) plotted as a function of the photon energy hυ. The fundamental absorption range of chalcogenide glasses is usually described by the Tauc relation:[46]

$$\alpha = \frac{A(h\upsilon - E_g)^2}{h\upsilon}, \quad (1)$$

where E_g is the optical band gap, and $A \approx 10^5$ cm^{-1} eV^{-1} is a constant. The experimental absorption data for g-Ga_2Te_3 above 1.5 eV are well described by eqn (1). The derived optical band gap E_g = 1.20 ± 0.02 eV is slightly higher than that for fcc Ga_2Te_3, 1.08 eV,[47,48] and similar to E_g for various amorphous counterparts, 1.09–1.20 eV.[43-45]

3.2 Raman spectra

Typical Raman spectrum of vitreous Ga_2Te_3 PLD film is shown in Fig. 2 together with those of face-centered cubic Ga_2Te_3, bulk glassy $GaTe_3$ and amorphous Te.[18,49] The spectrum is reminiscent of both Te-rich glassy binaries and the cubic polymorph. The most intense spectral feature at 126 ± 1 cm^{-1} corresponds to the A_1 in-phase Ga-Te breathing in $GaTe_4$ tetrahedra, as it is shown by DFT modeling.[18] The two weak features at 185 and 230 cm^{-1} are similar to those in fcc Ga_2Te_3 and seem to be related to asymmetric Ga-Te stretching in $GaTe_4$ tetrahedra.[18] The second intense feature at 156 cm^{-1} is related to Te-Te stretching observed in amorphous tellurium and Te-rich glassy binaries.[18,49-51] The 156 cm^{-1} peak intensity is substantially reduced in the Ga_2Te_3 PLD layer compared to bulk Ga_xTe_{1-x} glasses, $0.17 \le x \le 0.25$. As expected, the Te-Te stretching is missing in cubic Ga_2Te_3. The Raman results imply a chemical disorder in the vitreous PLD film, that is, the presence of both Te-Te and Ga-Ga homopolar bonds in addition to the expected Ga-Te heteropolar counterparts.

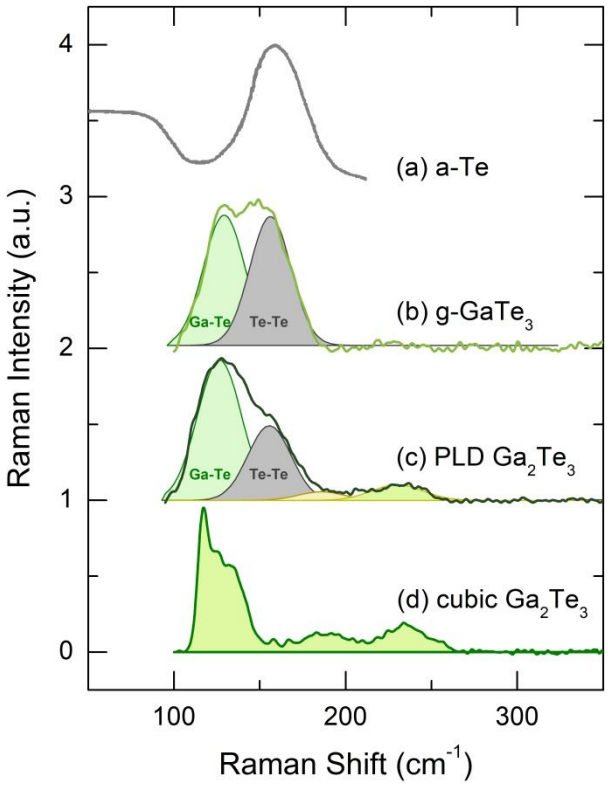

Fig. 2 Raman spectra in the Ga-Te system: (a) amorphous Te,[49] (b) bulk glassy $GaTe_3$ (x = 0.25),[18] (c) vitreous Ga_2Te_3 PLD film (this work), and (d) cubic Ga_2Te_3,[18] space group $F\bar{4}3m$.[11] The A_1 in-phase Ga-Te breathing and Te-Te stretching are highlighted in light green and light gray, respectively. See text for further details.

3.3 High-energy X-ray diffraction

The Faber-Ziman X-ray structure factor $S_X(Q)$ of Ga_2Te_3 PLD thin film is shown in Fig. 3(a,b) in comparison with bulk glassy $GaTe_3$ (x = 25 at.% Ga):[18]

$$S_X(Q) = w_{GaGa}(Q)S_{GaGa}(Q) + w_{GaTe}(Q)S_{GaTe}(Q) + w_{TeTe}(Q)S_{TeTe}(Q), \quad (2)$$

where $w_{ij}(Q)$ are Q-dependent X-ray weighting coefficients and $S_{ij}(Q)$ the Faber-Ziman partial structure factors. In contrast to the last vitreous alloy revealing some weak Bragg peaks[18] of cubic Ga_2Te_3, space group $F\bar{4}3m$,[11] the PLD film is completely amorphous. The $S_X(Q)$ shows rather intense first sharp diffraction peak (FSDP) at Q_0 = 0.86 ± 0.01 Å^{-1}, similar to those in bulk Ga_xTe_{1-x} glasses, $0.17 \le x \le 0.25$.[18] The FSDP amplitude $A_0(Q)$ increases with x and shifts to lower Q, the inset in Fig. 3(a). The first and second principle peaks (PP1, PP2) at Q_1 = 1.89 Å^{-1} and Q_2 = 3.20 Å^{-1} are also slightly shifted to lower scattering vectors, simultaneously increasing in intensity, compared to bulk glassy $GaTe_3$.

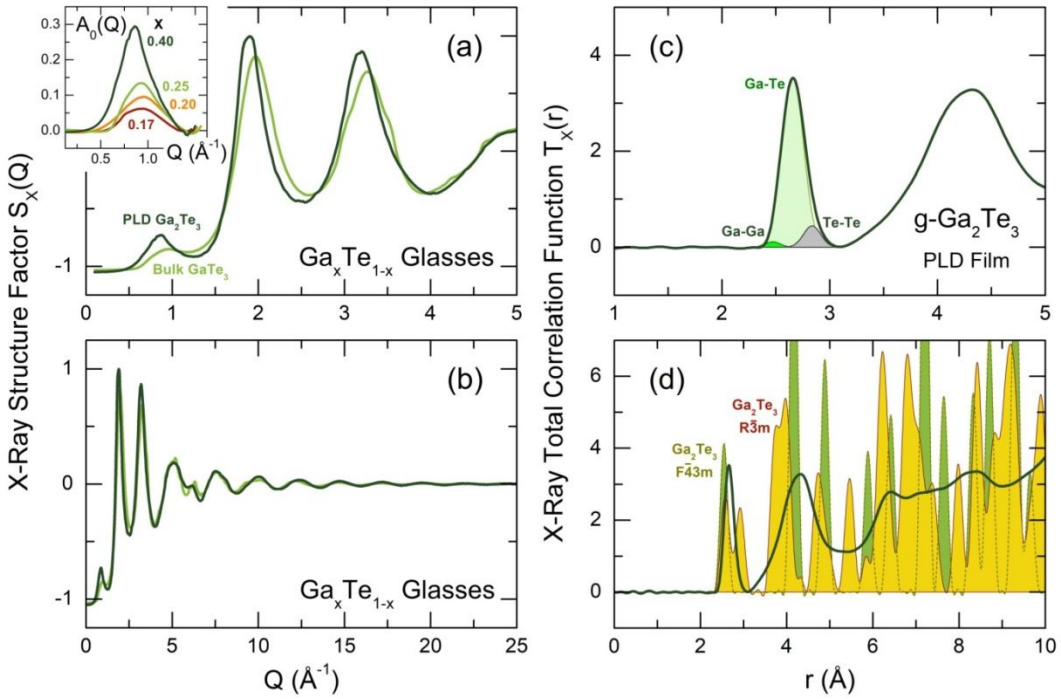

Fig. 3 High-energy X-ray diffraction data for glassy Ga_2Te_3 PLD film: X-ray structure factor $S_X(Q)$ over (a) limited and (b) extended Q-range plotted together with $S_X(Q)$ for bulk glassy $GaTe_3$ (x = 0.25);[18] (c) a constrained three-peak Gaussian fitting of the nearest neighbor (NN) feature in the total correlation function $T_X(r)$ for vitreous Ga_2Te_3 film; the Ga-Ga, Ga-Te and Te-Te NN correlations are highlighted in bright green, light green and light grey, respectively; and (d) $T_X(r)$ functions for the Ga_2Te_3 PLD film, cubic ($F\bar{4}3m$)[11] and rhombohedral ($R\bar{3}m$)[52] Ga_2Te_3 polymorphs. The inset shows the compositional evolution of the first sharp diffraction peak (FSDP) for bulk Ga_xTe_{1-x} glasses and Ga_2Te_3 PLD film (x = 0.40).

The X-ray total correlation function $T_X(r)$, obtained through the usual Fourier transform, is shown in Fig. 3(c,d)

$$T_X(r) = 4\pi\rho_0 r + \frac{2}{\pi}\int_0^{Q_{max}} Q[S_X(Q) - 1]\sin QrM(Q)\mathrm{d}Q, \qquad (3)$$

where ρ_0 is the experimental number density, $M(Q)$ the Lorch window function, and Q_{max} = 25 Å^{-1}. The $T_X(r)$ exhibits an asymmetric peak at 2.65 Å, mostly related to the Ga-Te nearest neighbors (NN), a broad poorly resolved second neighbor peak at 4.3 Å, and more distant unresolved correlations between 6.4 and 8.3 Å. The $T_X(r)$ shape is reminiscent of the ambient cubic ($F\bar{4}3m$)[11] and the high-pressure rhombohedral ($R\bar{3}m$)[52] Ga_2Te_3 polymorphs taking into account a significant broadening of the real-space functions for the amorphous PLD film.

A two-peak Gaussian fitting of the asymmetric NN feature, suggesting only Ga-Te contributions, yields the gallium coordination number N_{GaTe} > 4. Taking into account the Raman results, Fig. 2, the presence of Te-Te atomic pairs implies the appearance of Ga-Ga NN counterparts. A constrained three-peak fitting, imposing the mixed tetrahedral Ga environment, $N_{GaX} = N_{GaGa} + N_{GaTe}$ = 4, and mixed tellurium coordination, $N_{TeX} = N_{TeTe} + N_{TeGa}$, gives reasonable local coordination numbers: 0.30 (Ga-Ga), 3.70 (Ga-Te), 0.28 (Te-Te), Table 1, with a rather small chemical disorder $\chi = N_{GaGa}/N_{GaX} \approx N_{TeTe}/N_{TeX}$ = 8.8 ± 1.3%. The derived χ value is significantly lower than that in vitreous As_2Te_3, χ = 30-35%,[53-57] in accordance with hetero- and homopolar bond energy differences: E_{Ga-Te} = 147 kJ mol^{-1} > ½($E_{Ga-Ga} + E_{Te-Te}$) = 120 kJ mol^{-1}, while

E_{As-Te} = ½(E_{As-As} + E_{Te-Te}) = 136 kJ mol^{-1},[58] see Electronic Supplementary Information (ESI) for further details. The obtained partial N_{GaGa} and N_{GaTe} coordination, as well as the Ga-Ga and Ga-Te NN separations are consistent with the EXAFS results.[17] The derived interatomic distances: 2.47 Å (Ga-Ga), 2.66 Å (Ga-Te), and 2.83 Å (Te-Te) are also in accordance with crystalline references[11,52,59,60] and Te-rich binary and ternary vitreous alloys.[18,61,62]

Table 1 Nearest-neighbor interatomic distances r_{ij} and partial coordination numbers N_{ij} in experimental and FPMD data for glassy Ga_2Te_3 PLD film

Ga-Ga		Ga-Te		Te-Te		N_{Ga-X}	N_{Te-X}
r_{Ga-Ga} (Å)	N_{Ga-Ga}	r_{Ga-Te} (Å)	N_{Ga-Te}	r_{Te-Te} (Å)	N_{Te-Te}		
Experimental X-ray data							
2.47(1)	0.30(3)	2.66(1)	3.70(5)	2.83(2)	0.28(5)	4.00(6)	2.75(9)
FPMD data							
2.45(1)	0.25(2)	2.63(1)	3.71(4)	2.82(2)	0.27(4)	3.96(5)	2.75(7)

3.4 First-principles simulations

The first-principles molecular dynamics (FPMD) using a GGA/PBE0 hybrid functional enables a good agreement with experimental diffraction data, Fig. 4(a,b), observed earlier for different chalcogenide systems.[18,27-29] The derived interference function $Q[S_X(Q) - 1]$ reproduces well both the $S_X(Q)$ oscillations at high scattering vectors and the amplitude and peak positions at lower Q. The PP1 height at Q_1 = 1.89 Å^{-1} appears to be slightly underestimated, a typical situation for relatively small FPMD simulation boxes.[27,63] The simulated real-space correlation functions are also mimic well the experimental results, Fig. 4(b), ensuring reliable description of the short- and intermediate-range order. The partial structure factors $S_{ij}(Q)$ are presented in Fig. 4(c). We note an intense FSDP at 0.85 Å^{-1} for the $S_{GaGa}(Q)$ function, responsible for the experimental low-Q feature in spite of the small X-ray weighting, $\langle w_{GaGa}(Q)\rangle$ = 0.0662 ± 0.0012, where the angle brackets denote averaging over the applied Q-range.

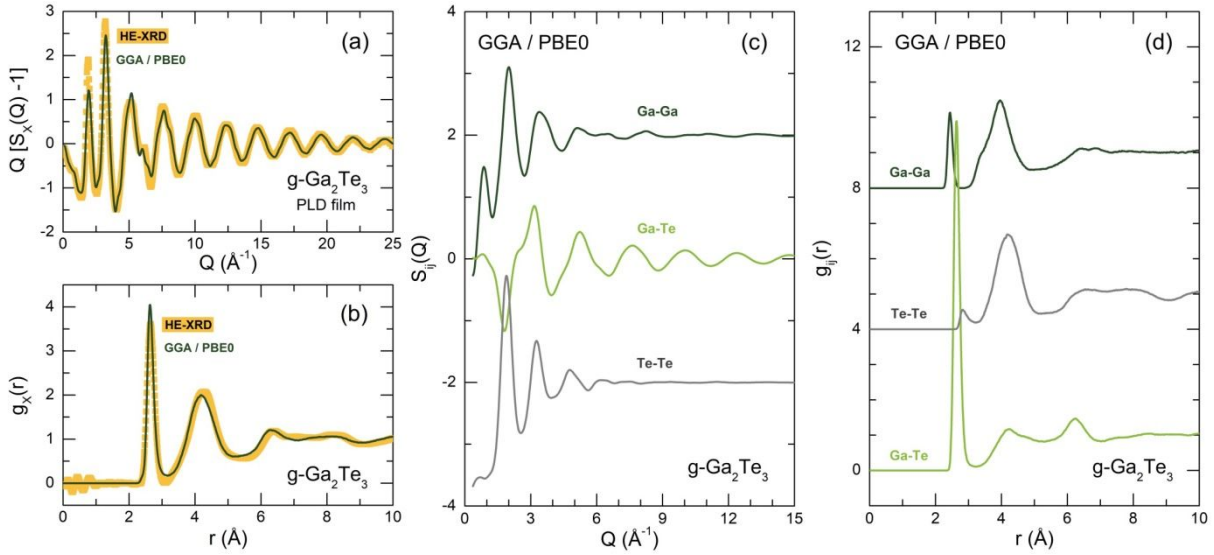

Fig. 4 GGA/PBE0 simulation results for vitreous Ga_2Te_3 PLD film. Experimental and simulated (a) X-ray interference function $Q[S_X(Q)-1]$ and (b) pair-distribution function $g_X(r)$; (c) partial Faber-Ziman structure factors $S_{ij}(Q)$; and (d) partial pair-distribution functions $g_{ij}(r)$.

The simulated partial pair-distribution functions $g_{ij}(r)$ are given in Fig. 4(d). Both the Ga-Ga and Te-Te NN features are clearly seen at 2.45 and 2.82 Å, respectively, consistent with Raman, Fig. 2, and diffraction, Fig. 3(c), data. The derived interatomic distances and partial coordination numbers are summarized in Table 1 and are in excellent agreement with high-energy X-ray diffraction results. We should also note a low-r shoulder at 3.36 Å for the Ga-Ga second neighbor peak, corresponding to edge-sharing (ES) Ga-Te polyhedra. The fraction of the ES-units appears to be f_{ES} = 0.42 ± 0.03.

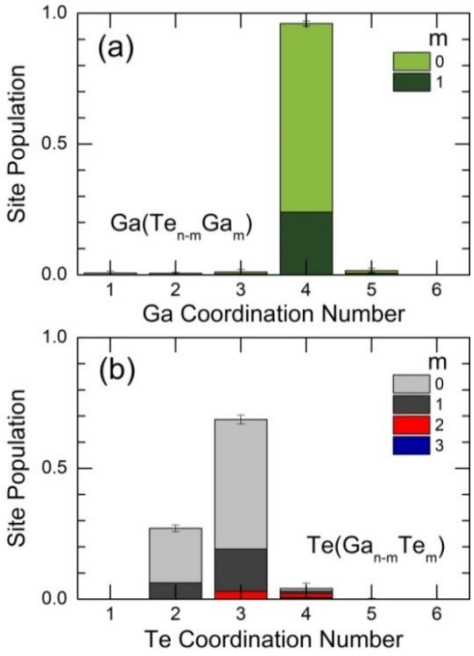

Fig. 5 GGA/PBE0 calculated (a) gallium and (b) tellurium local coordination numbers. Light green and light gray colors highlight pure Ga-Te and Te-Ga fractions in Ga($Te_{n-m}Ga_m$) or Te($Ga_{n-m}Te_m$) polyhedra (m = 0), respectively. Dark green and dark gray tones correspond to m = 1. Bright red and blue colors denote populations of Te-rich homopolar Te($Ga_{n-m}Te_m$) units, $m \geq 2$.

The calculated distributions of Ga and Te local coordination numbers are shown in Fig. 5. Gallium is essentially four-fold coordinated; the population of under- and over-coordinated species is negligible, $p_{Ga \neq 4} \approx 0.04$. The average tellurium coordination is N_{Te-X} = 2.75, and trigonal Te appears to be a clear majority, 69 ± 2%. Chain-like tellurium sites have the second-largest population, 27 ± 2%, while the fraction of 4-fold coordinated tellurium, Te_{4F}, is just 4 ± 2%.

Pure heteropolar Ga($Te_{n-m}Ga_m$) or Te($Ga_{n-m}Te_m$) environment, m = 0, exhibits approximately three-quarters of gallium and tellurium. Local configurations with one homopolar pair, m = 1, reveal 23-26% of the both species. The Te-rich homopolar environments Te($Ga_{n-m}Te_m$), $m \geq 2$, are rare, 5 ± 2%.

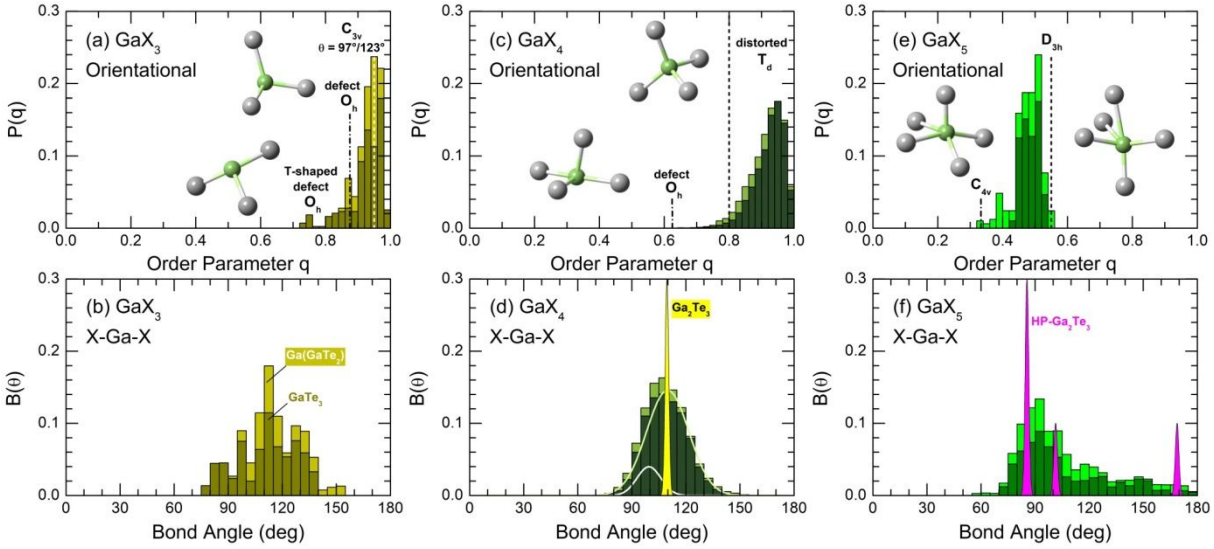

Fig. 6 Orientational order parameter q and X-Ga-X bond angle distribution $B_{\mathrm{XGaX}}(\theta)$, where X = Te or Ga for (a,b) GaX_3, (c,d) GaX_4, and (e,f) GaX_5 polyhedra. The insets show typical shapes of Ga-Te entities. The $B_{\mathrm{TeGaTe}}(\theta)$ distributions for cubic (yellow) and rhombohedral (magenta) Ga_2Te_3 are also shown. The parameters of pure heteropolar units $GaTe_3$, $GaTe_4$ and $GaTe_5$ are highlighted in dark colors; their mixed counterparts are pale-colored.

The topology of Ga-centered polyhedra is given by the X-Ga-X bond angle distribution $B_{\mathrm{XGaX}}(\theta)$, where X = Te or Ga, and by the order parameter q,[64,65] extended beyond the tetrahedral geometry[66]

$$q = 1 - \frac{3}{8}\sum_{j=1}^{n-1}\sum_{k=j+1}^{n}\left(\cos\psi_{jk} + \frac{1}{3}\right)^2, \qquad (4)$$

where ψ_{jk} is the X-Ga-X angle of a given GaX_n unit. The average value of q changes between 0 for an ideal gas and q = 1 for a regular tetrahedral network (n = 4).

The $B_{\mathrm{XGaX}}(\theta)$ for 4-fold coordinated gallium is shown in Fig. 6(d). A nearly symmetric broad distribution is centered at θ = 109.9° ± 0.5° and indicates a predominantly tetrahedral geometry of GaX_4 units, similar to that in cubic Ga_2Te_3.[11] In addition to the major $B_{\mathrm{XGaX}}(\theta)$ component, one observes a hidden lower-θ supplement at 99.5° ± 0.4° suggesting either strongly distorted GaX_4 tetrahedra or a non-tetrahedral topology. The orientational order parameter q confirms the tetrahedral shape of GaX_4, Fig. 6(c). The asymmetric $P(q)$ probability distribution function is peaked at q = 0.95 and exhibits a long tail toward lower q. Usually, the low-q tetrahedral limit is estimated to be at $q \approx 0.8$, followed by a defect octahedral environment over the range $0.4 \lesssim q \lesssim 0.8$.[29,66] The regular defect octahedron GaX_4 with two missing X species and the bond angles $\theta_{O_h}(1) = \pi/2$ and $\theta_{O_h}(2) = \pi$ is characterized by q = 5/8, located just in the middle of this q-range. The $P(q)$ integration using the above q-limit yields the tetrahedral fraction f_{T_d} = 0.97 ± 0.02. There is no substantial change in geometry for pure $GaTe_4$ and mixed GaX_4 tetrahedra, whose parameters are highlighted in Fig. 6(c,d) by dark and light green colors, respectively.

The geometry of under- GaX_3 and over-coordinated GaX_5 minorities is also analyzed in Fig. 6. The trigonal GaX_3 entities usually have a pyramidal shape of the approximate C_{3v} symmetry, the inset in Fig. 6(a). The corresponding $P(q)$ probability distribution is peaked at q = 0.95

suggesting the average trigonal angle $\langle\theta_{C_{3v}}\rangle$ = 97° or $\langle\theta_{C_{3v}}\rangle'$ = 123°, since the $P(q)$ function for regular C_{3v} pyramids has a quasi-symmetric shape peaked at the tetrahedral angle θ_{T_d} = 109.47° with a maximum of q = 1. The bond angle distribution $B_{\mathrm{XGaX}}(\theta)$ is consistent with this conclusion, Fig. 6(b). The defect octahedra GaX_3 have two possible configurations: (i) the C_{3v} shape with $\theta_{O_h}(1) = \pi/2$, q = 7/8; and (ii) the planar T-shape of the C_{2v} symmetry with $\theta_{O_h}(1) = \pi/2$ and $\theta_{O_h}(2) = \pi$ angles, q = 3/4. The both varieties exhibit non-monotonic "bumps" on a rather smooth $P(q)$.

The over-coordinated GaX_5 entities have two expected geometries related either to (1) a regular square pyramid C_{4v}, q = 1/3, or to (2) a trigonal bipyramid D_{3h}, $q \approx 0.55$, see the insets in Fig. 6(e). The calculated $P(q)$ distribution is located between these two limits assuming that the glass structural motif is an intermediate case. Basically, both the C_{4v} and D_{3h} species represent a defect and/or distorted octahedral environment. Consequently, it is not surprising that the bond angle distribution for GaX_5 polyhedra appears to be reminiscent of $B_{\mathrm{TeGaTe}}(\theta)$ for high-pressure rhombohedral Ga_2Te_3 with octahedral gallium coordination,[52] Fig. 6(f).

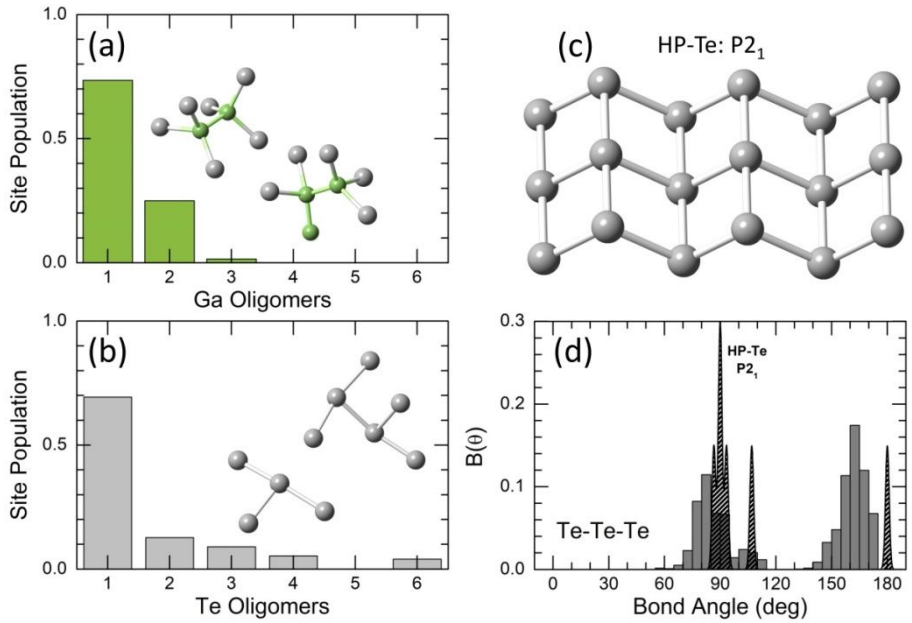

Fig. 7 Gallium and tellurium oligomers in g-Ga_2Te_3: the size distribution of (a) Ga_n and (b) Te_n oligomers, (c) structural motif of high-pressure monoclinic HP-Te II, space group $P2_1$,[67] (d) the bond angle distribution $B_{\mathrm{TeTeTe}}(\theta)$ in Te_3 and higher Te_n oligomers, n > 3, in comparison with that for HP-Te II. The insets show typical shapes of Ga_n and Te_n oligomers.

The observed and simulated chemical disorder raises a question of the structural arrangement for the Ga-Ga and Te-Te atomic pairs. The connectivity analysis shows the Ga-Ga occurrence mostly in the form of dimers, Fig. 7(a). The population of gallium trimers is lower by a factor of ≈20. In contrast, the Te-Te contacts have a wider variability arising as Te_n oligomers, where $2 \le n \le 6$, Fig. 7(b). The tellurium trimers and higher oligomers, $n \ge 3$, reveal unexpected bond angle distribution, similar to $B_{\mathrm{TeTeTe}}(\theta)$ in high-pressure monoclinic HP-Te II, space group $P2_1$,[67] Fig. 7(d).

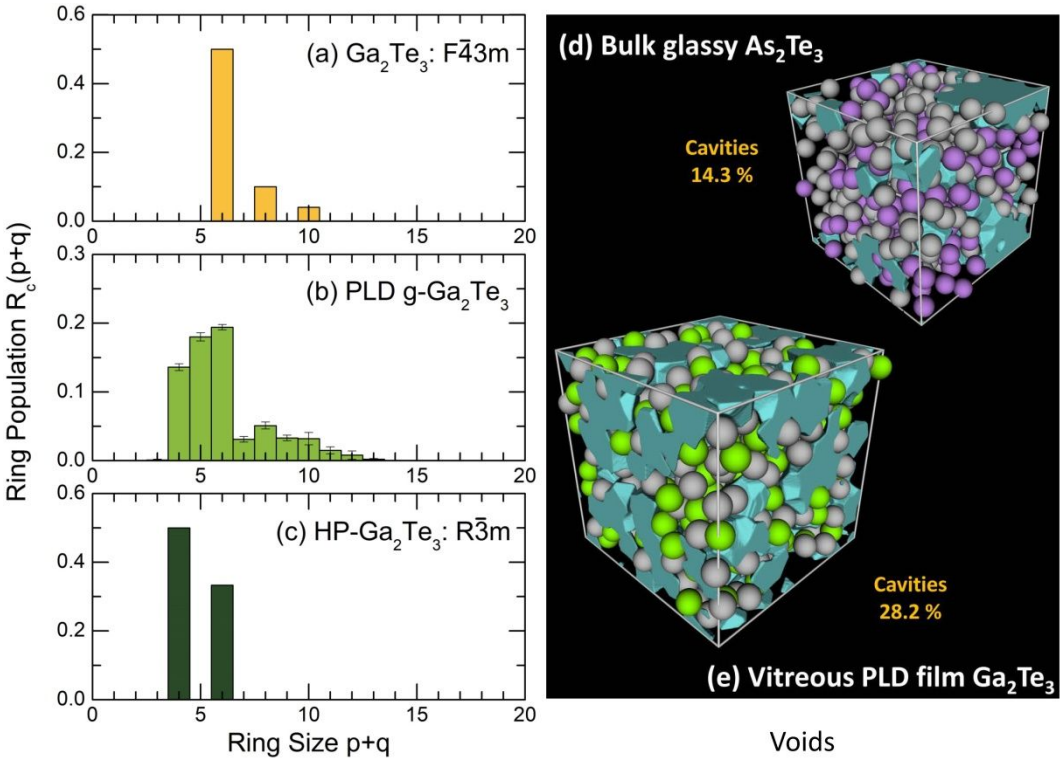

Fig. 8 Rings and cavities in vitreous Ga_2Te_3. Ring statistics $R_c(p+q)$[39] in (a) ambient pressure cubic,[11] (b) glassy (this work), and (c) high-pressure rhombohedral[52] Ga_2Te_3 polymorphs. Cavities in (d) bulk glassy As_2Te_3 (preliminary results) and (e) vitreous Ga_2Te_3 PLD thin film.

The intermediate-range order in vitreous Ga_2Te_3 is given by Ga_pTe_q ring statistics. The ring population $R_c(p+q)$[39] is shown in Fig. 8 in comparison with those for the cubic and rhombohedral Ga_2Te_3 polymorphs. The $R_c(p+q)$ for glassy Ga_2Te_3 is roughly bimodal. The populated small rings, $4 \le p+q \le 6$, coexist with a wide distribution of less frequent bigger Ga_pTe_q units, $7 \le p+q \le 13$, broadly centered at $p+q = 9 \pm 1$. Basically, the ring statistics in g-Ga_2Te_3 represents a disordered mixture of $R_c(p+q)$ for the ambient and high-pressure gallium sesquitelluride polymorphs.

Microscopic cavities in vitreous Ga_2Te_3, calculated using the Dirichlet-Voronoi tessellation,[41] are shown in Fig. 8 together with those in bulk glassy As_2Te_3 (preliminary results). The voids fraction V_c, normalized to the volume of the FPMD simulation box, 28.2 ± 0.3%, is very similar to that in glassy $Ga_{0.2}Te_{0.8}$.[18] In contrast, bulk vitreous As_2Te_3 of the same stoichiometry and with similar As atomic size has a much lower V_c = 14.3 ± 0.2%, that is, by a factor of 2 smaller. The origin of this difference is not completely clear since glassy gallium and arsenic sesquisulfides reveal comparable cavity fractions, 38.4 vs. 44.1%, respectively.[27,58] Chemically disordered As_2Te_3 may have a denser packing possibly related to lower bonding constraints while homopolar ½(As-As+Te-Te) and heteropolar As-Te bonding energies are nearly identical, see section 3.3 and ESI. Another explanation may be related to a different bonding character in respective crystalline sesquitellurides reflected in amorphous counterparts. Rhombohedral β-As_2Te_3 shows typical characteristics of metavalent solids:[68] large Born effective charge, high optical dielectric constant, low Debye temperature, and a metal-like electrical conductivity, in contrast to cubic Ga_2Te_3. The non-metavalent properties of the latter, however, can be transformed under high pressure, as it is shown for monoclinic α-As_2S_3.[69]

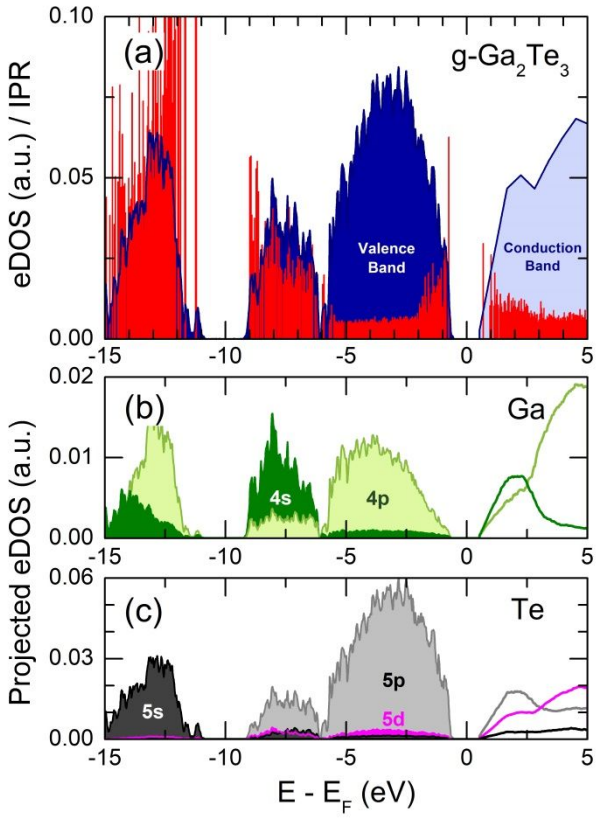

Fig. 9 Electronic properties of glassy Ga_2Te_3: (a) the electronic density of states (eDOS) and the inverse participation ratio (IPR, red spikes); the projected eDOS on (b) Ga s and p, and (c) Te s, p and d atomic pseudo-wave functions. See text for further details.

The total electronic density of states (eDOS) calculated from the Kohn-Sham eigenvalue spectra is shown in Fig. 9. The derived valence band structure is typical for glassy and crystalline chalcogenides[55,70-72] and consists of three sub-bands between the Fermi energy E_F and −15 eV. The upper part, centered at −3 eV, is predominately populated by the Te 5p and Ga 4p states, shown by the eDOS projections on Ga and Te atomic pseudo-wave functions. The sub-band peaked at −7.5 eV mostly contains comparable contributions of the Te 5p and Ga 4s components. Finally, the lower band at −13 eV essentially has an s-character related to the Te 5s elections together with the Ga 4s and 4p states. As expected, the Ga species reveal hybrid s–p electron states over the entire valence band energy range, presumably of the average sp^3 stoichiometry, since the s– and p–related orbitals are appearing and changing simultaneously in all three sub-bands. Surprisingly, the tellurium electron states are also hybridized revealing 5s, 5p and 5d contributions. In addition, one observes some admixture of the Ga 4d and 4f states to the hybrid sp^3 orbitals, not shown in Fig. 9 because of the weak gallium 4d and 4f orbital population. Similar hybridization of the Ti 3d, 4s, and 4p states, and of the O 2s and 2p orbitals on each site was already reported for rutile, TiO_2, using site-specific XPS analysis and DFT simulations,[73] even if Ti^{4+} was expected to have empty valence band electron states. The Te 5p nonbonding electron component, usually located at −2±1 eV in the top of the valence band,[55,72,74,75] is hardly visible in Fig. 9, since the tellurium lone-pair electrons are substantially transferred to the gallium sp^3 hybrid orbitals because of insufficient number of the Ga valence electrons: $4s^2 4p^1$. In case of Te-rich bulk glassy $GaTe_4$,[18] the Te 5p nonbonding states are clearly distinguishable as a shoulder at −1.5 eV (Fig. S2 in ESI).

The derived eDOS is consistent with experimental XPS data[76] and similar to that for glassy In_2Te_3.[72] As expected, vitreous Ga_2Te_3 appears to be semiconducting with the derived band gap E_g^{PBE0} = 1.48 eV, slightly overestimated compared to the experimental value, 1.20 eV, Fig. 1, and reported results.[43-45]

The inverse participation ratio (IPR)[74,75] characterizes the degree of localization of a single-particle Kohn-Sham eigenfunction $\psi(\boldsymbol{r})$

$$\mathrm{IPR} = \frac{\int d\boldsymbol{r}|\psi(\boldsymbol{r})|^4}{\left(\int d\boldsymbol{r}|\psi(\boldsymbol{r})|^2\right)^2}. \quad (5)$$

A small IPR value ($\propto N^{-1}$, where N is the number of atoms in the simulation box) corresponds to an extended wave function, while a large IPR $\rightarrow$ 1 indicates a strong localization around specific covalent bond. The calculated IPRs, derived using the projections of $\psi(\boldsymbol{r})$ onto an atomic basis set and the atomic orbital coefficients, are shown in Fig. 9, plotted together with the eDOS. We note a higher electron localization at the band tails (the top of the valence and the bottom of the conduction bands), consistent with the theories of disordered semiconductors.[77] The remaining electron states in the vicinity of the energy gap are delocalized. On the contrary, the deeper states of Ga 4s and Te 5s character appear to be even more strongly localized, participating in the covalent bonding. Similar situation was reported for many tellurides.[70,72,74,75]

3.5 Multilevel optical changes induced by laser pulses

Preliminary pump-probe optical experiments have confirmed low-power reversible phase-change transitions in Ga_2Te_3 PLD thin films, reported previously only for electrical switching.[8-10] A single 532 nm nanosecond pulse of appropriate energy density crystallizes the amorphous material completely, decreasing the optical transmission $T(t)$, Fig. 10(a), and increasing the reflection $R(t)$. The required limit of the energy density is quite low, 20 mJ cm^{-2} even at λ_{pump} = 800 nm, Fig S3 (ESI); the 100 nm Ga_2Te_3 film is rather transparent for photons with 800 nm wavelength, Fig. 1. The energy density of 50 mJ cm^{-2} at λ_{pump} = 532 nm is slightly above the SET threshold. While crystallizing, the normalized transmittance $T(t)/T_a$, where T_a is the transmission of the amorphous film, exhibits a minimum (-16%) at $t \approx 40$ ns and then increases reaching a plateau (-12%) above 150 ns. The observed non-monotonic behavior can be related to a local heating, induced by the nanosecond pulse, and/or to a partial re-amorphization. Pulses with higher energy density, 65 mJ cm^{-2} at λ_{pump} = 532 nm, gradually restore the RESET logic state (a complete re-amorphization), Fig. 10(b), with the corresponding decrease of the normalized reflectivity, $R(t)/R_c$, where R_c is the reflectivity of fully crystallized Ga_2Te_3 layer. The difference in $R(t)/R_c$ between a- and c-Ga_2Te_3 reaches -58%. These preliminary results can be compared with a rough estimation of the expected changes in optical transmission and reflection related to a density change between amorphous (5.22 g cm^{-3}) and cubic Ga_2Te_3 (5.64 g cm^{-3}) and leading to a change in the refractive index (calculation details are given in ESI). The expected decrease in $T(t)/T_a$ for crystalline Ga_2Te_3 is -8%, while $R(t)/R_c$ is expected to decrease by -19% on re-amorphization. These estimations show that a density change alone is insufficient to explain the observed changes in optical properties of Ga_2Te_3 during reversible phase transformations. The magnitude of the observed changes in reflectivity and transmittance is

comparable with those in GeTe.[78-80] A multilevel writing seems to be realized here, simply controlled by the number of appropriate nanosecond pulses.

These preliminary optical measurements without any optimization and with relatively thick samples show promising PCM response of gallium sesquitelluride, which seems to be comparable with that of classical PCMs, see, for example, recent papers and reviews[81-84] and references therein. A meticulous choice of the laser operation parameters, substrates, optimal thicknesses, etc. will substantially improve the PCM performance. Further optical experiments are in progress and will be reported elsewhere.

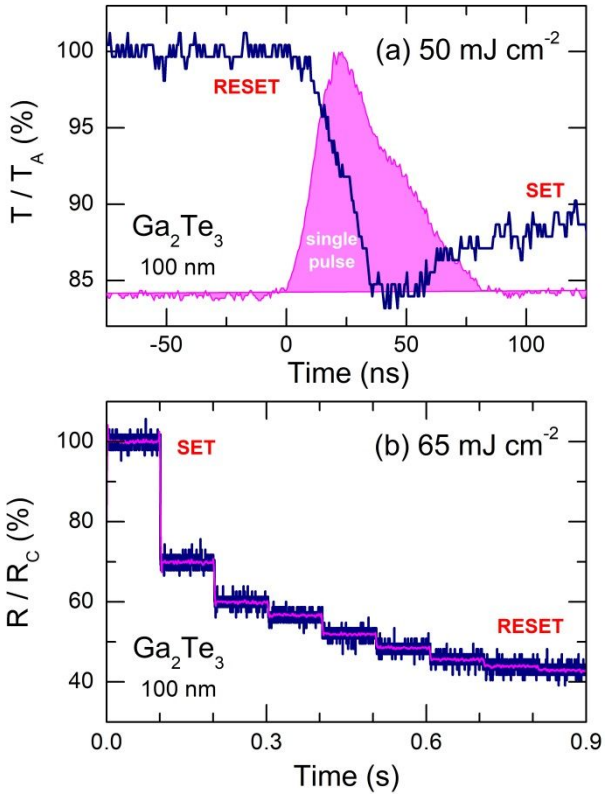

Fig. 10 Optical SET-RESET transitions in Ga_2Te_3 PLD films (100 nm) induced by a nanosecond laser with λ_{pump} = 532 nm: (a) a single pulse with the energy density 50 mJ cm^{-2} (transmission mode); (b) a multi-pulse train with the energy density 65 mJ cm^{-2} (reflection mode) and the repetition rate 10 Hz. The temporary profile of a single laser pulse (highlighted in pink) is also shown in (a). The smoothed reflectivity data of the sample re-amorphization (the pink curve) is shown in (b). See text for further details.

In addition to future systematic pump-probe experiments, we are also planning spectroscopic ellipsometry measurements on both amorphous and crystallized Ga_2Te_3 thin films, providing important complementary data on dielectric functions and optical response,[12] X-ray reflectometry experiments to evaluate the density and thickness changes,[85] and optical absorption measurements on crystallized Ga_2Te_3 samples.

3.6 Atomic structure, nanotectonic nuclei and the origin of optical and electrical contrast in Ga_2Te_3

In contrast to flagship PCMs as GeTe or $Ge_2Sb_2Te_5$, gallium tellurides are characterized by the sp^3 hybridization of gallium and the absence of Peierls distortion. Consequently, the phase-change mechanisms are expected to be different compared to classical fast transformers.[17] Basically, the atomic structure of vitreous Ga_2Te_3 seems to be similar to the cubic polymorph: the gallium environment is predominantly tetrahedral, and the tellurium local coordination N_{TeX} = 2.75 ± 0.08 is very close to the fcc value, $N_{\mathrm{TeX}}^{\mathrm{fcc}}$ = 2⅔. The only significant differences appear to be a substantial fraction of edge-sharing tetrahedra ES-$GaTe_4$, f_{ES} = 0.42 ± 0.03, and the observed chemical disorder, χ = 0.088 ± 0.013. As a result, the expected changes in optical and electronic properties are suggested to be relatively small and do not predict strong PCM response. Nevertheless, the preliminary pump-probe laser experiments and the reported electrical switching results[8-10] indicate a good electrical and optical contrast between the SET and RESET states.

We note, however, that the SET logic state should not necessarily be related to the stable ambient pressure polymorph. For example, the crystalline SET counterpart of GeTe has a metastable rock-salt lattice and is not the stable rhombohedral modification.[3] Likewise, high-pressure rhombohedral Ga_2Te_3, metastable at ambient conditions, can be crystallized from a supercooled liquid after appropriate laser or electric pulses of suitable duration and energy density.

Rhombohedral high-pressure HP-Ga_2Te_3, space group $R\bar{3}m$,[52] is very different from typical gallium chalcogenides having the tetrahedral structure. This crystal belongs to Bi_2Te_3 structural type whose structure consists of repeated quintuple layers of atoms, Te2–Ga–Te1–Ga–Te2 stacking along the *c* axis of the unit cell (Figure S4). The gallium local coordination is octahedral with two different Ga-Te distances: 2.58 Å and 2.92 Å, while tellurium is four-fold coordinated in average (Te1 is octahedrally coordinated and two Te2 have trigonal coordination: $\langle N_{\mathrm{Te-Ga}} \rangle$ = (6 + 3 × 2)/3 = 4. The Peierls distortion of rhombohedral HP-Ga_2Te_3 with two different Ga-Te nearest neighbor separations is clearly seen for the neutron total correlation function $T_{\mathrm{N}}(r)$, Fig. S5, calculated from the cif file[52] using the XTAL code.[86]

The question arises why a high pressure polymorph is expected to be formed in these conditions. A possible answer is related to a very unusual phenomenon, the nanotectonic compression, recently found for Te-rich bulk glassy $GaTe_3$ on heating above the glass transition temperature T_{g}.[18] The reported *in situ* XRD measurements as a function of temperature have shown a simultaneous co-crystallization of both ambient and high pressure polymorphs: (a) trigonal tellurium and monoclinic HP-Te II, stable above 4 GPa,[67] and (b) fcc Ga_2Te_3 and rhombohedral HP-Ga_2Te_3, usually co-existing between 5 and 8 GPa.[52] The emergence of HP-forms is a consequence of two factors: the presence of high-pressure nuclei in the supercooled liquid and their growth with increasing temperature promoted by high internal pressure, reaching 4 to 8 GPa. A drastic difference in thermal expansion coefficients between the incipient HP-nuclei and the rigid and viscous supercooled liquid seems to be the origin of nanotectonic compression in gallium tellurides, resulting in crystallization of metallic HP-phases.

The obtained FPMD results for vitreous Ga_2Te_3 and preliminary data for supercooled and normal gallium sesquitelluride liquids are consistent with this scenario. The incipient HP-nuclei related to both monoclinic Te II and rhombohedral Ga_2Te_3 were found in the glassy PLD film. Their fraction is negligible at room temperature, 2-4% (Figs. 5-7), but increases rapidly above T_{g}, ensuring the appearance of HP-crystallites and then of the HP-polymorphs. In addition, vitreous

Ga_2Te_3 has a number of more or less distinct resemblances with HP-Ga_2Te_3, such as the ring statistics, Fig. 8, or the presence of the ES-units, absent in fcc Ga_2Te_3, providing a transformation path into HP-polymorph at the intermediate range scale. The metallic high-pressure forms are beneficial for PCM performance and energy consumption ensuring higher electrical and optical contrast for a given energy density of incoming laser or electric pulses. We should also note that rhombohedral HP-Ga_2Te_3 has some characteristic properties of incipient metals:[87] (1) it is isostructural to Bi_2Te_3, a typical metavalent sesquitelluride,[68] (2) it has a moderate conductivity,[88] ≈10 S cm^{-1}, and (3) its effective coordination number does not obey the $(8–N)$ rule.

Additional information related to structural SET-RESET and RESET-SET changes is given in ESI. Further studies of laser-induced SET-RESET phenomena and related structural transformations are necessary to verify this hypothesis and a long-term stability of nonvolatile memory and photonic devices based on atypical phase change alloy Ga_2Te_3.

4 Conclusions

Vitreous stoichiometric Ga_2Te_3 thin films with a thickness of 1.10 μm and 100 nm were obtained by pulsed laser deposition for structural, optical and phase-change pump-probe laser experiments. The films were found to be homogeneous and uniform with the optical band gap E_g = 1.20 ± 0.02 eV and the refractive index n_R = 3.13 ± 0.08 over the 1.1 ≤ λ ≤ 2.3 μm spectral range.

Raman spectroscopy and high-energy X-ray diffraction supported by first-principles molecular dynamics with the hybrid functional GGA/PBE0 have shown a slightly distorted four-fold gallium coordination with the tetrahedral fraction f_{T_d} = 0.97 ± 0.02 and a negligible population of under- and over-coordinated Ga species $p_{Ga\neq 4}$ ≈ 0.04. Both the experimental and FPMD simulated results revealed a mixed gallium and tellurium local environment consisting of heteropolar Ga-Te/Te-Ga and homopolar Ga-Ga/Te-Te bonds. The chemical disorder χ at room temperature was found to be rather small, $\chi = N_{GaGa}/N_{GaX} \approx N_{TeTe}/N_{TeX}$ = 8.8 ± 1.3%, where X = Ga or Te, consistent with a significant bond energy differences: E_{Ga-Te} = 147 kJ mol^{-1} > ½(E_{Ga-Ga}+E_{Te-Te}) = 120 kJ mol^{-1}.

The calculated electronic density of states was similar to the reported experimental results and exhibits the energy gap E_g^{PBE0} = 1.48 eV, that is, slightly overestimated compared to the fundamental optical absorption edge. The inverse participation ratio indicates a stronger localization at the valence and conduction band tails, while the remaining electronic states appear to be extended, consistent with the theories of disordered semiconductors. Both the gallium and tellurium valence band orbitals are hybridized; the gallium hybridization has presumably a sp^3 character.

The derived atomic structure of vitreous Ga_2Te_3 PLD film and of the stable ambient pressure fcc polymorph are quite similar. The important differences include the presence of a substantial fraction of edge-sharing units, f_{ES} = 0.42 ± 0.03, absent in the cubic crystal, the chemical disorder and a small part, 2-4%, of incipient nanotectonic nuclei. The latter are reminiscent of monoclinic HP-Te II, stable above 4 GPa, and rhombohedral HP-Ga_2Te_3, coexisting with the fcc

polymorph between 5 and 8 GPa. The metastable HP-Ga_2Te_3 with octahedral gallium local environment and metavalent bonding seems to form the SET logic state in atypical Ga_2Te_3 PCM capable of multilevel writing. Further studies are necessary to verify this hypothesis.

The preliminary optical pump-probe laser experiments have shown promising high-contrast, fast and reversible PCM response of gallium sesquitelluride, previously observed only for electrical switching. Further optimization of the laser operation parameters, substrates, film thicknesses, etc. is expected improving substantially the PCM performance of Ga_2Te_3 and related materials.

Conflicts of interest

There are no conflicts to declare.

Acknowledgements

This work was supported by the Ministry of Science and Higher Education under agreement 075-15-2019-1950 and 075-15-2021-917; state assignment FSRC 'Crystallography and Photonics' Russian Academy of Sciences. The work at the Advanced Photon Source, Argonne National Laboratory, was supported in part by the Office of Basic Energy Sciences, US Department of Energy, under Contract no. DE-AC02-06CH1135. The work at Tallinn University of Technology (Estonia) was supported by the European Union through the European Regional Development Fund project 'Center of Excellence' TK141. The optical measurements in part were carried out in the resource center of St. Petersburg State University: 'Center for Optical and Laser Materials Research'. The FPMD simulations were carried out using the HPC computing resources at Lomonosov Moscow State University and at the ILIT RAS in Shatura (Moscow Region). This work was also granted access to the HPC resources of IDRIS (France) under the allocation 2020-A0090910639 made by GENCI (Grand Equipement National de Calcul Intensif) and using the CALCULCO computing platform, supported by SCoSI/ULCO (Service COmmun du Système d'Information de l'Université du Littoral Côte d'Opale).

References

1 M. Wuttig and N. Yamada, Phase-change materials for rewriteable data storage, *Nat. Mater*., 2007, **6**, 824–832.

2 S. Raoux, W. Wełnic and D. Ielmini, Phase change materials and their application to nonvolatile memories, *Chem. Rev*., 2010, **110**, 240–267.

3 A. V. Kolobov and J. Tominaga, *Chalcogenides: Metastability and Phase Change Phenomena*, Springer, Berlin, 2012, pp 149–267.

4 W. Zhang, R. Mazzarello, M. Wuttig and E. Ma, Designing crystallization in phase-change materials for universal memory and neuro-inspired computing, *Nat. Rev. Mater*., 2019, **4**, 150–168.

5 C. Ríos, N. Youngblood, Z. Cheng, M. Le Gallo, W. H. P. Pernice, C. D. Wright, A. Sebastian, H. Bhaskaran, In-memory computing on a photonic platform, *Sci. Adv*., 2019, **5**, eaau5759.

6 M. Xu, X. Mai, J. Lin, W. Zhang, Y. Li, Y. He, H. Tong, X. Hou, P. Zhou, and X. Miao, Recent advances on neuromorphic devices based on chalcogenide phase-change materials, *Adv. Func. Mater*., 2020, **30**, 2003419.

7 J. Feldmann, N. Youngblood, M. Karpov, H. Gehring, X. Li, M. Stappers, M. Le Gallo, X. Fu, A. Lukashchuk, A. S. Raja, J. Liu, C. D. Wright, A. Sebastian, T. J. Kippenberg, W. H. P. Pernice, and H. Bhaskaran, Parallel convolutional processing using an integrated photonic tensor core, *Nature*, 2021, **589**, 52–61.

8 H. Zhu, J. Yin, Y. Xia and Z. Liu, Ga_2Te_3 Phase change material for low-power phase change memory application, *Appl. Phys. Lett*., 2010, **97**, 083504.

9 D. Lee, T. Kim and H. Sohn, Highly reliable threshold switching behavior of amorphous Ga_2Te_3 films deposited by RF sputtering, *Appl. Phys. Express*, 2019, **12**, 085504.

10 D. Lee, T. Kim, J. Kim, and H. Sohn, Effect of nitrogen doping on threshold voltage in amorphous Ga_2Te_3 for application of selector devices, *Phys. Stat. Solidi A*, 2020, **217**, 2000478.

11 M. Guymont, A. Tomas and M. Guittard, The structure of Ga_2Te_3. An X-ray and high-resolution electron microscopy study, *Philos. Mag. A*, 1992, **66**, 133–139.

12 K. Shportko, S. Kremers, M. Woda, D. Lencer, J. Robertson, and M. Wuttig, Resonant bonding in crystalline phase-change materials, *Nat. Mater*., 2008, **7**, 653–658.

13 B. J. Kooi and M. Wuttig, Chalcogenides by design: Functionality through metavalent bonding and confinement, *Adv. Mater*., 2020, **32**, 1908302.

14 L. Guarneri, S. Jakobs, A. von Hoegen, S. Maier, M. Xu, M. Zhu, S. Wahl, C. Teichrib, Y. Zhou, O. Cojocaru-Mirédin, M. Raghuwanshi, C.-F. Schön, M. Drögeler, C. Stampfer, R. P. S. M. Lobo, A. Piarristeguy, A. Pradel, J.-Y. Raty, and M. Wuttig, Metavalent bonding in crystalline solids: How does it collapse? *Adv. Mater*., 2021, **33**, 2102356.

15 S. Takeda, S. Tamaki and Y. Waseda, Local ordering features in the structure of liquid Ga-Te alloys, *J. Phys. Soc. Jpn*, 1983, **52**, 2062–2071.

16 P. Buchanan, A. C. Barnes, K. R. Whittle, M. A. Hamilton, A. N. Fitch and H. E. Fischer, A determination of the structure of liquid Ga_2Te_3 using combined X-ray diffraction and neutron diffraction with isotopic substitution, *Mol. Phys*., 2001, **99**, 767–772.

17 A. V. Kolobov, P. Fons, M. Krbal, K. Mitrofanov, J. Tominaga, and T. Uruga, Local structure of the crystalline and amorphous states of Ga_2Te_3 phase-change alloy without resonant bonding: A combined X-ray absorption and ab initio study, *Phys. Rev. B*, 2017, **95**, 054114.

18 M. Bokova, A. Tverjanovich, C. J. Benmore, D. Fontanari, A. Sokolov, M. Khomenko, M. Kassem, I. Ozheredov, and E. Bychkov, Unraveling the atomic structure of bulk binary Ga−Te glasses with surprising nanotectonic features for phase-change memory applications, *ACS Appl. Mater. Interfaces*, 2021, **13**, 37363−37379.

19 V. V. Ionin, A. V. Kiselev, N. N. Eliseev, V. A. Mikhalevsky, M. A. Pankov, and A. A. Lotin, Multilevel reversible laser-induced phase transitions in GeTe thin films, *Appl. Phys. Lett*., 2020, **117**, 011901.

20 N. N. Eliseev, A. V. Kiselev, V. V. Ionin, V. A. Mikhalevsky, A. A. Burtsev, M. A. Pankov, D. N. Karimov, and A. A. Lotin, Wide range optical and electrical contrast modulation by laser-induced phase transitions in GeTe thin films, *Res. Phys*., 2020, **19**, 103466.

21 A. V. Kiselev, V. A. Mikhalevsky, A. A. Burtsev, V. V. Ionin, N. N. Eliseev and A. A. Lotin, Transmissivity to reflectivity change delay phenomenon observed in GeTe thin films at laser-induced reamorphization, *Optics Laser Techn*., 2021, **143**, 107305.

22 A. P. Hammersley, S. O. Svensson, M. Hanfland, A. N. Fitch, and D. Häusermann, Two-dimensional detector software: from real detector to idealised image or two-theta scan, *High Pressure Res*., 1996, **14**, 235−248.

23 L. B. Skinner, C. J. Benmore and J. B. Parise, Area detector corrections for high quality synchrotron X-ray structure factor measurements, *Nucl. Instrum. Methods Phys. Res*., 2012, **662**, 61−70.

24 J. Hutter, M. Iannuzzi, F. Schimann, and J. VandeVondele, CP2K: Atomistic simulations of condensed matter systems, *Wiley Interdiscip. Rev.: Comput. Mol. Sci*., 2014, **4**, 15−25.

25 J. P. Perdew, M. Ernzerhof and K. Burke, Rationale for mixing exact exchange with density functional approximations, *J. Chem. Phys*., 1996, **105**, 9982−9985.

26 C. Adamo and V. Barone, Toward reliable density functional methods without adjustable parameters: the PBE0 model, *J. Chem. Phys*., 1999, **110**, 6158−6170.

27 A. Tverjanovich, M. Khomenko, S. Bereznev, D. Fontanari, A. Sokolov, T. Usuki, K. Ohara, D. Le Coq, P. Masselin, and E. Bychkov, Glassy GaS: Transparent and Unusually Rigid Thin Films for Visible to Mid-IR Memory Applications. *Phys. Chem. Chem. Phys*. 2020, **22**, 25560−25573.

28 M. Kassem, T. Bounazef, D. Fontanari, A. Sokolov, M. Bokova, A. C. Hannon, and E. Bychkov, Chemical and structural variety in sodium thioarsenate glasses studied by neutron diffraction and supported by first-principles simulations, *Inorg. Chem*. 2020, **59**, 16410−16420.

29 A. Tverjanovich, M. Khomenko, C. J. Benmore, M. Bokova, A. Sokolov, D. Fontanari, M. Kassem, T. Usuki, and E. Bychkov, Bulk glassy $GeTe_2$: a missing member of the tetrahedral GeX_2 family and a precursor for the next generation of phase-change materials, *Chem. Mater*. 2021, **33**, 1031−1045.

30 S. Grimme, S. Ehrlich, and L. Goerigk, Effect of the damping function in dispersion corrected density functional theory, *J. Comput. Chem*., 2011, **32**, 1456−1465.

31 M. Micoulaut, Communication: Van der Waals corrections for an improved structural description of telluride based materials, *J. Chem. Phys*., 2013, **138**, 061103.

32 A. Bouzid, C. Massobrio, M. Boero, G. Ori, K. Sykina, and E. Furet, Role of the van der Waals interactions and impact of the exchange-correlation functional in determining the structure of glassy $GeTe_4$, *Phys. Rev. B*, 2015, **92**, 134208.

33 J. Akola, R. O. Jones, S. Kohara, S. Kimura, K. Kobayashi, M. Takata, T. Matsunaga, R. Kojima and N. Yamada, Experimentally constrained density-functional calculations of the amorphous structure of the prototypical phase-change material $Ge_2Sb_2Te_5$, *Phys. Rev. B*, 2009, **80**, 020201.

34 T. Matsunaga, J. Akola, S. Kohara, T. Honma, K. Kobayashi, E. Ikenaga, R. O. Jones, N. Yamada, M. Takata and R. Kojima, From local structure to nanosecond recrystallization dynamics in AgInSbTe phase-change materials, *Nat. Mater*., 2011, **10**, 129–134.

35 O. Gereben and L. Pusztai, RMC_POT, a computer code for Reverse Monte Carlo modeling the structure of disordered systems containing molecules of arbitrary complexity, *J. Comput. Chem*., 2012, **33**, 2285–2291.

36 (a) S. Goedecker, M. Teter and J. Hutter, Separable dual-space Gaussian pseudopotentials, *Phys. Rev. B*, 1996, **54**, 1703–1710; (b) C. Hartwigsen, S. Goedecker and J. Hutter, Relativistic separable dual-space Gaussian pseudopotentials from H to Rn, *Phys. Rev. B*, 1998, **58**, 3641–3662.

37 S. Nosé, A molecular dynamics method for simulations in the canonical ensemble, *Mol. Phys*., 1984, **52**, 255–268.

38 W. G. Hoover, Canonical dynamics: equilibrium phase-space distributions, *Phys. Rev. A*, 1985, **31**, 1695–1697.

39 S. Le Roux and P. Jund, Ring statistics analysis of topological networks: new approach and application to amorphous GeS_2 and SiO_2 systems, *Comput. Mater. Sci*., 2010, **49**, 70–83.

40 S. Kohara, H. Ohno, M. Tabaka, T. Usuki, H. Morita, K. Suzuya, J. Akola and L. Pusztai, Lead silicate glasses: binary network-former glasses with large amounts of free volume, *Phys. Rev. B*, 2010, **82**, 134209.

41 I. Heimbach, F. Rhiem, F. Beule, D. Knodt, J. Heinen and R. O. Jones, pyMolDyn: identification, structure, and properties of cavities/vacancies in condensed matter and molecules, *J. Comput. Chem.*, 2017, **38**, 389–394.

42 R. Swanepoel, Determination of the thickness and optical constants of amorphous silicon, *J. Phys. E: Sci. Instrum*., 1983, **16**, 1214–1222.

43 S. Ozaki, K. Takada and S. Adachi, Optical constants of amorphous Ga_2Te_3 and In_2Te_3, *Jpn. J. Appl. Phys*., 1994, **22**, 6213–6217.

44 A. E. Bekheet, Electrical and optical properties of amorphous Ga_2Te_3 films, *Eur. Phys. J.: Appl. Phys*. 2001, **16**, 187–193.

45 M. Popescu, F. Sava, A. Lörinczi, A. Velea, I. D. Simandan, A. C. Galca, E. Matei, G. Socol, F. Gherendi, D. Savastru, and S. Miclos, Amorphous thin films in the gallium–chalcogen system, *Phys. Stat. Solidi B*, 2016, **253**, 1033–1037.

46 J. Tauc, Optical properties of amorphous semiconductors, in *Amorphous and Liquid Semiconductors*, ed. J. Tauc, Plenum, London, 1974, pp 159–220.

47 G. Harbeke and G. Lautz, Zur Ultrarotabsorption van Galliumtelluride (Ga_2Te_3) und Indiumtellrid (In_2Te_3), *Z. Naturforsch. A*, 1958, **13**, 775–779.

48 S. Sen and D. N. Bose, Electrical and optical properties of single crystal In_2Te_3 and Ga_2Te_3, *Solid State Commun*., 1984, **50**, 39–42.

49 M. H. Brodsky, R. J. Gambino, J. E. Smith, Jr. and Y. Yacoby, The Raman spectrum of amorphous tellurium. *Phys. Stat. Solidi*, 1972, **52**, 609–614.

50 A. Tverjanovich, K. Rodionov, and E. Bychkov, Raman spectroscopy of glasses in the As–Te system, *J. Solid State Chem*., 2012, **190**, 271–276.

51 A. Tverjanovich, A. Cuisset, D. Fontanari, and E. Bychkov, Structure of Se-Te glasses by Raman spectroscopy and DFT modelling, *J. Am. Ceram. Soc*., 2018, **101**, 5188–5197.

52 N. R. Serebryanaya, The crystal structure of pressure-induced phases of In_2Te_3 and Ga_2Te_3, *Powder Diffr*., 1992, **7**, 99–102.

53 Q. Ma, D. Raoux and S. Bénazeth, Local structure of As_xTe_{100-x} glasses studied by differential X-ray anomalous scattering and X-ray-absorption spectroscopy, *Phys. Rev. B*, 1993, **48**, 16332–16346.

54 Y. Kumeda, T. Usuki and O. Uemura, TOF-neutron diffraction study of liquid Tl-As_2X_3 systems (X: Se, Te), *J. Non-Cryst. Solids*, 1996, **205–207**, 130–134.

55 C. Otjacques, J.-Y. Raty, F. Hippert, H. Schober, M. Johnson, R. Céolin, and J.-P. Gaspard, Structural and vibrational study of the negative thermal expansion in liquid As_2Te_3, *Phys. Rev. B*, 2010, **82**, 054202.

56 D. C. Kaseman, I. Hung, K. Lee, K. Kovnir, Z. Gan, B. Aitken, and S. Sen, Tellurium speciation, connectivity, and chemical order in As_xTe_{100-x} glasses: results from two-dimensional ^{125}Te NMR spectroscopy, *J. Phys. Chem. B*, 2015, **119**, 2081–2088.

57 V. V. Brazhkin, E. Bychkov and O. B. Tsiok, As_2Te_3 glass under high hydrostatic pressure: Polyamorphism, relaxation, and metallization, *Phys. Rev. B*, 2017, **95**, 054205.

58 E. Soignard, O. B. Tsiok, A. S. Tverjanovich, A. Bytchkov, A. Sokolov, V. V. Brazhkin, C. J. Benmore, and E. Bychkov, Pressure-driven chemical disorder in glassy As_2S_3 up to 14.7 GPa, postdensification effects, and applications in materials design, *J. Phys. Chem. B*, 2020, **124**, 430–442.

59 M. Julien-Pouzol, S. Jaulmes and F. Alapini, Tellurure de gallium, *Acta Crystallogr. B*, 1977, **33**, 2270–2272.

60 H. J. Deiseroth, P. Amann and H. Thurn, Die Pentatelluride M_2Te_5 (M = Al, Ga, In): Polymorphie, Strukturbeziehungen und Homogenitätsbereiche, *Z. Anorg. Allg. Chem*., 1996, **622**, 985–993.

61 I. Voleská, J. Akola, P. Jóvári, J. Gutwirth, T. Wágner, T. Vasileiadis, S. N. Yannopoulos, and R. O. Jones, Structure, electronic, and vibrational properties of glassy $Ga_{11}Ge_{11}Te_{78}$: Experimentally constrained density functional study, *Phys. Rev. B*, 2012, **86**, 094108.

62 I. Pethes, A. Piarristeguy, A. Pradel, S. Michalik, R. Nemausat, J. Darpentigny, and P. Jóvári, Short range order and topology of $Ge_xGa_xTe_{100-2x}$ glasses, *J. Alloys Compd*., 2020, **834**, 155097.

63 T. Ohkubo, K. Ohara and E. Tsuchida, Conduction mechanism in $70Li_2S$-$30P_2S_5$ glass by ab initio molecular dynamics simulations: comparison with $Li_7P_3S_{11}$ crystal, *ACS Appl. Mater. Interfaces*, 2020, **12**, 25736–25747.

64 P.-L. Chau and A. J. Hardwick, A new order parameter for tetrahedral configurations, *Mol. Phys*., 1998, **93**, 511–518.

65 J. R. Errington and P. G. Debenedetti, Relationship between structural order and the anomalies of liquid water, *Nature*, 2001, **409**, 318–321.

66 S. Caravati, M. Bernasconi, T. D. Kühne, M. Krack and M. Parrinello, Coexistence of tetrahedral- and octahedral-like sites in amorphous phase change materials, *Appl. Phys. Lett.*, 2007, **91**, 171906.

67 (a) K. Aoki, O. Shimomura and S. Minomura, Crystal structure of the high-pressure phase of tellurium, *J. Phys. Soc. Jpn*., 1980, **48**, 551–556; (b) M. Takumi, T. Masamitsu and K. Nagata, X-ray structural analysis of the high-pressure phase III of tellurium, *J. Phys.: Condens. Matter*, 2002, **14**, 10609–10613.

68 Y. Cheng, O. Cojocaru-Mirédin, J. Keutgen, Y. Yu, M. Küpers, M. Schumacher, P. Golub, J.-Y. Raty, R. Dronskowski, and M. Wuttig, Understanding the structure and properties of sesquichalcogenides (i.e., V_2VI_3 or Pn_2Ch_3 (Pn = pnictogen, Ch = chalcogen) compounds) from a bonding perspective, *Adv. Mater*., 2019, **31**, 1904316.

69 V. P. Cuenca-Gotor, J. Á. Sans, O. Gomis, A. Mujica, S. Radescu, A. Muñoz, P. Rodríguez-Hernández, E. L. da Silva, C. Popescu, J. Ibañez, R. Vilaplana, F. J. Manjón, Orpiment under compression: metavalent bonding at high pressure, *Phys. Chem. Chem. Phys*., 2020, **22**, 3352–3369.

70 S. Blaineau and P. Jund, Electronic structure of amorphous germanium disulfide via density-functional molecular dynamics simulations, *Phys. Rev. B*, 2004, **70**, 184210.

71 J. Akola and R. O. Jones, Structural phase transitions on the nanoscale: The crucial pattern in the phase-change materials $Ge_2Sb_2Te_5$ and GeTe, *Phys. Rev. B*, 2007, **76**, 235201.

72 D. Dragoni, S. Gabardi and M. Bernasconi, First-principles study of the liquid and amorphous phases of In_2Te_3, *Phys. Rev. Mater*., 2017, **1**, 035603.

73 J. C. Woicik, E. J. Nelson, L. Kronik, M. Jain, J. R. Chelikowsky, D. Heskett, L. E. Berman and G. S. Herman, Hybridization and bond-orbital components in site-specific X-ray photoelectron spectra of rutile TiO_2, *Phys. Rev. Lett*., 2002, **89**, 077401.

74 J. Kalikka, J. Akola, R. O. Jones, S. Kohara and T. Usuki, Amorphous $Ge_{15}Te_{85}$: density functional, high-energy X-ray and neutron diffraction study, *J. Phys.: Condens. Matter*, 2012, **24**, 015802.

75 S. Caravati, M. Bernasconi and M. Parrinello, First-principles study of liquid and amorphous Sb_2Te_3, *Phys. Rev. B*, 2010, *81*, 014201.

76 K. Tamura, M. Misonou and H. Endo, Electrical resistivity of liquid Te, Ga_2Te_3, In_2Te_3 and Tl_2Te under high pressure, *J. Phys. Soc. Japan*, 1979, **46**, 637–642.

77 N. F. Mott and E. A. Davis, *Electronic Processes in Non-Crystalline Materials*, 2nd ed., Clarendon Press, Oxford, 1979, pp 22–27.

78 S. Raoux, H.-Y. Cheng, M. A. Caldwell, and H.-S. P. Wong, Crystallization times of Ge–Te phase change materials as a function of composition, *Appl. Phys. Lett*., 2009, **95**, 071910.

79 W. Gawelda, J. Siegel, C. N. Afonso, V. Plausinaitiene, A. Abrutis, and C. Wiemer, Dynamics of laser-induced phase switching in GeTe films, *J. Appl. Phys*., 2011, **109**, 123102.

80 X. Sun, A. Lotnyk, M. Ehrhardt, J. W. Gerlach, and B. Rauschenbach, Realization of multilevel states in phase-change thin films by fast laser pulse irradiation, *Adv. Optical Mater*., 2017, **5**, 1700169.

81 J. Zheng, A. Khanolkar, P. Xu, S. Colburn, S. Deshmukh, J. Myers, J. Frantz, E. Pop, J. Hendrikson, J. Doylend, N. Boechler and A. Majumdar, GST-on-silicon hybrid nanophotonic integrated circuits: a non-volatile quasi-continuously reprogrammable platform, *Opt. Mater. Express*, 2018, **8**, 1551–1561.

82 N. Farmakidis, N. Youngblood, X. Li, J. Tan1, J. L. Swett, Z. Cheng, C. D. Wright, W. H. P. Pernice, and H. Bhaskaran, Plasmonic nanogap enhanced phase-change devices with dual electrical-optical functionality, *Sci. Adv*., 2019, **5**, eaaw2687.

83 H. Zhang, L. Zhou, J. Xu, N. Wang, H. Hu, L. Lu, B. M. A. Rahman, J. Chen, Nonvolatile waveguide transmission tuning with electrically-driven ultra-small GST phase-change material, *Sci. Bull*., 2019, **64**, 782–789.

84 S. Abdollahramezani, O. Hemmatyar, H. Taghinejad, A. Krasnok, Y. Kiarashinejad, M. Zandehshahvar, A. Alù and A. Adibi, Tunable nanophotonics enabled by chalcogenide phase-change materials, *Nanophotonics*, 2020, **9**, 20200039.

85 W. K. Njoroge, H-W. Wöltgens, and M. Wuttig, Density changes upon crystallization of $Ge_2Sb_{2.04}Te_{4.74}$ films, *J. Vac. Sci. Technol. A*, 2002, **20**, 230–233.

86 A. C. Hannon, XTAL: a Program for Calculating Interatomic Distances and Coordination Numbers for Model Structures. Rutherford-Appleton Laboratory Report RAL-93-063 (1993) 16 pp. ; http://wwwisis2.isis.rl.ac.uk/disordered/ACH/Software/xtal.htm .

87 M. Wuttig, V. L. Deringer, X. Gonze, C. Bichara, and J.-Y. Raty, Incipient metals: Functional materials with a unique bonding mechanism, *Adv. Mater*., 2018, **30**, 1803777.

88 V. V. Shchennikov, K. V. Savchenko, and S. V. Popova, Electrical properties of the high-pressure phases of gallium and indium tellurides, Phys. Solid State, 2000, 42, 1036–1040.